Journal of Computational Physics 228 (2009) 6349–6360

Contents lists available at ScienceDirect

Journal of Computational Physics

journal homepage: www.elsevier.com/locate/jcp

Mesh refinement algorithms in an unstructured solver for multiphase flow simulation using discrete particles

Yuanhong Li, Song-Charng Kong *

Department of Mechanical Engineering, Iowa State University, 2025 Black Engineering Building, Ames, IA 50011, USA

ARTICLE INFO

Article history:
Received 18 December 2008
Received in revised form 3 April 2009
Accepted 14 May 2009
Available online 19 May 2009

Keywords:
Adaptive mesh refinement
Spray modeling
Grid dependence
Unstructured solver

ABSTRACT

This study developed spray-adaptive mesh refinement algorithms with directional sensitivity in an unstructured solver to improve spray simulation for internal combustion engine application. Inadequate spatial resolution is often found to cause inaccuracies in spray simulation using the Lagrangian–Eulerian approach due to the over-estimated diffusion and inappropriate liquid–gas phase coupling. Dynamic mesh refinement algorithms adaptive to fuel sprays and vapor gradients were developed in order to increase the grid resolution in the spray region to improve simulation accuracy. The local refinement introduced the coarse-fine face interface that requires advanced numerical schemes for flux calculation and grid rezoning with moving boundaries. To resolve the issue in flux calculation, this work implemented the refinement/coarsening algorithms into a collocated solver to avoid tedious interpolations in solving the momentum equations. A pressure correction method was applied to address unphysical pressure oscillations due to the collocation of pressure and velocity. An edge-based algorithm was used to evaluate the edge-centered quantities in order to account for the contributions from all the cells around an edge at the coarse-fine interface. A quasi-second-order upwind scheme with strong monotonicity was also modified to accommodate the coarse-fine interface for convective fluxes. To resolve the issue related to grid rezoning, rezoning was applied to the initial baseline mesh only and the new locations of the refined grids were obtained by interpolating the updated baseline mesh. The time step constraints were also re-evaluated to account for the change resulting from mesh refinement. The present refinement algorithm was used in simulating fuel sprays in an engine combustion chamber. It was found that the present approach could produce the same level of results as those using the uniformly fine mesh with substantially reduced computer time. Results also showed that this approach could alleviate the artifacts related to the Lagrangian discrete modeling of spray drops due to insufficient spatial resolution.

1. Introduction

Modeling fuel sprays in internal combustion engines is a challenging task due to the complex physical processes involved. For dilute sprays, a commonly used approach is based on the Lagrangian discrete particle method [1] in which the properties of representative droplet parcels are randomly chosen from empirical or theoretical distribution functions. The continuous gas phase is described using an Eulerian method. Liquid–gas interactions are modeled by the coupling source terms for the exchange of mass, momentum, energy and turbulence. Various sub-models are used to describe the droplet breakup,

* Corresponding author. Tel.: +1 515 294 3244; fax: +1 515 294 3261.
E-mail address: kong@iastate.edu (S.-C. Kong).

0021-9991/$ - see front matter © 2009 Elsevier Inc. All rights reserved.
doi:10.1016/j.jcp.2009.05.018

collision, turbulent dispersion, evaporation and wall interaction [2–7]. The accuracy of simulation results not only relies on the fidelity of the models but also on the temporal and spatial resolutions of the governing equations.

Numerous numerical studies have indicated that spray simulation is subject to the influence of the grid resolution and the mesh type [8–15]. The grid dependence can be partially attributed to the inadequate spatial resolution of the coupling between the gas and liquid phases. In the region near the injector exit, the velocity and species density gradients can be strong when a high-velocity spray is injected into a slowly moving gas. Inadequate space resolution in the spray region can result in a much higher relative velocity between the gas and liquid and an over-estimation of diffusion [16]. The higher relative velocity then affects the liquid penetration and vaporization since the relative velocity is used to calculate spray breakup and vaporization. Thus the use of a fine mesh is often required in the region near the injector to improve spray modeling, while the use of a coarser mesh is recommended away from the injector to save computer time.

Grid resolution also inherently affects the performance of various spray sub-models [8–16]. The stochastic collision algorithm [3] adopted in many CFD codes inevitably depends on the grid resolution since the algorithm only allows parcels within the same cell to collide. Collision probability in this algorithm also depends on the grid resolution, since the cell volume is considered in the calculation. In evaporation calculation, fuel vapor is assumed to be uniformly distributed within a computational cell. This treatment can result in over-estimated vapor diffusion (lower vapor density) because the vapor mass fraction in the cell is compared to that at the droplet surface to determine evaporation rate [17]. Furthermore, the statistical convergence of the stochastic discrete approach may not be guaranteed or may progress very slowly, and a better phase coupling is needed [8].

While improving the sub-models to reduce the grid dependence has attracted much attention [12–21], the improvements may still be subject to further validation and tuning of model constants for specific conditions. Another way to obtain more accurate spray simulations is to increase the spatial resolution. However, the volume of the droplets inside a cell should be small enough compared to the cell volume in order to satisfy the dilute spray assumption for the Lagrangian liquid phase description. A uniformly fine mesh is limited not only by the available computer power but also by the flexibility of choosing grid resolution to meet the Lagrangian assumption.

Adaptive mesh refinement (AMR) [21–23] can be utilized to increase the spatial resolution in the spray region to improve the phase coupling and to alleviate the mesh dependence without incurring a significant computational cost. In particular, AMR can provide a greater flexibility in adapting to highly transient spray with adequate spatial resolution that otherwise would not be readily available if a uniformly fine mesh is used. A goal of this study was to develop AMR algorithms to simulate transient engine sprays in the unstructured KIVA-4 code [24], earlier versions of which have been widely used in the engine research community. The original KIVA-4 adopted a staggered approach for solving momentum equations and density-based equations for compressible flows. To simplify the numerical scheme and implementation for using AMR, this paper adopted a collocated approach in which velocity is solved at the cell center for the momentum equations and used for the gas–liquid coupling terms. A pressure correction method proposed by Rhie and Chow [25] was used to address unphysical pressure oscillations due to the collocation of pressure and velocity [26].

The current AMR approach determined data structure and numerical methods based on the features of the KIVA-4 solver. This approach attached new child cells to the existing cells and used a hierarchical structure to establish relationship between the parent cell and its child cells. The refined cells were coarsened to reduce computational cost if a higher grid density was not required. These dynamic procedures were controlled by using an adaptation criterion that incorporated the normalized fuel mass within a computational cell and the gradients of vapor mass fraction.

AMR requires advanced numerical methods to deal with the coarse-fine face interface where cells in different refinement levels meet. The calculation of diffusive fluxes needs to consider all the active cell edges for the edge-centered quantities and consider all the active cell faces for the surface fluxes. Note that a regular hexahedral cell consists of only 12 edges by definition. On the coarse-fine interface, one edge is divided into two edges. Therefore, the total number of edges of a coarse cell at the interface increases as a result of mesh refinement, and all the edges need to be considered in calculating the edge-centered values. On the other hand, the convective fluxes were determined from the second-order upwind scheme that meets strong monotone conditions to prevent under-shoot and over-shoot of the fluxes. Face normal velocities of the refined cells at the interface were utilized to advance the Lagrangian cell volume change in the pressure iteration and in the convective fluxing.

The remainder of this paper is organized as follows. In Section 2, mesh refinement algorithms along with the adaptation criteria are presented. In Section 3, *the numerical methods* dealing with the coarse-fine interface are described, followed by Section 4 in which numerical tests are performed to validate AMR implementation and demonstrate the benefits of spray simulations using AMR. Conclusions are summarized in Section 5.

2. Spray-adaptive mesh refinement algorithms

The current adaptation increases the grid density by splitting a cell into smaller child cells. This method provides flexibilities in the mesh construction and is consistent with the characteristics of the finite volume solver with the arbitrarily unstructured mesh [27]. The adaptation starts with an initial coarse mesh (level 0) and creates new grids with higher levels (level l) continuously as the computation progresses. Meanwhile, the refined grids are coarsened to the lower-level grids if the fine grid is not needed in order to reduce the computational cost.

In this study, the adaptation was performed on a hexahedral mesh that is commonly used in engine simulations. The adaptation criteria are based on normalized liquid fuel mass and fuel vapor gradients as will be described in Section 2.2. If a cell met the criteria, it was tagged and divided into 2^d(d is the dimension) sub-cells or child cells as shown in Fig. 1(a). If all the child cells of a parent cell met the coarsening criteria, all the child cells of the parent cell were de-activated and the parent cell was restored. The detailed procedures are described as follows.

2.1. Refinement/coarsening algorithms

The refinement involved grid creation, connectivity setup and property update. The procedure consisted of the following steps:

(1) Insert new vertices on each edge, face and cell by interpolation to create new sub-edges, sub-faces and sub-cells.
(2) Establish relationship between the parent cell (level-($l-1$)) and its direct child cells (level-l).
(3) Deactivate the parent cell and update the connectivity.
(4) Relocate spray particles from the parent cell to the corresponding child cells based on the physical location.
(5) Determine the cell-centered properties of the child cells using the linear variation with local conservation.

For instance, a generic variable Q_c defined on the cell center of a child cell can be obtained by the linear variation of the function over the parent cell as

$$Q_c = Q_p + (\mathbf{x_c} - \mathbf{x_p}) \cdot (\nabla Q)_p \tag{1}$$

where Q_p is the value at the parent cell and $\mathbf{x_c}$, $\mathbf{x_p}$ are the cell center locations of the child cell and parent cell, respectively. $(\nabla Q)_p$ is the gradient evaluated on the parent cell using the least-squares method [28].

If all the child cells of a parent cell met the coarsening criteria, all these child cells were de-activated and the parent cell was restored. The coarsening procedure consisted of the following steps:

(1) Update the connectivity data.
(2) Relocate spray particles in the child cells to their parent cell.
(3) Determine the properties of the parent cell from the child cells by volume average or mass average satisfying conservation laws.

2.2. Refinement/coarsening criteria

Modeling of fuel–air mixing was influenced by the grid density in *twofold*. In the two-way coupling of the gas and liquid, the cell-centered gas quantities such as velocity and vapor concentration were used to calculate the gas-to-liquid coupling terms. On the other hand, the liquid-to-gas coupling terms were uniformly distributed over the computational cell. The grid size in the vicinity of liquid droplets influenced the fidelity of the two-way coupling. Reducing the cell size could improve the coupling calculations. Thus, it was reasonable and natural to choose spray-related quantities as the refinement criteria. It is also important to have good grid resolution near the injector exit since this will affect the later stage of the spray evolution. This paper adopted a criterion using the combination of "normalized fuel mass" and "vapor mass fraction gradients". The normalized fuel mass was the ratio of total mass of liquid and vapor (m_{l+v}) in a cell to the total injected fuel mass (m_{inj}) as

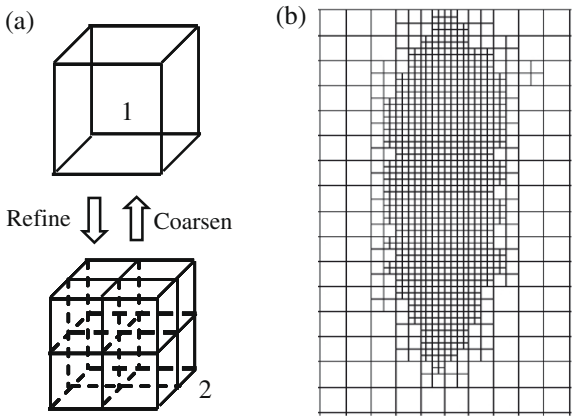

Fig. 1. (a) Schematic of mesh refining and coarsening and (b) a sample of adaptive mesh.

$$r_m = \frac{m_{l+v}}{m_{inj}}. \tag{2}$$

Because a majority of injected fuel was still in liquid at the beginning of injection, this criterion could ensure the proper adaptation in the region near the injector nozzle. The vapor gradients, *which refer to the gradients of the fuel vapor mass fraction at a cell center*, were also chosen in order to provide adequate grid resolution outside the spray periphery, where the vapor gradients were high. First derivatives were used to calculate the adaptation indicator from the vapor gradients as

$$\tau_{c,j} = \left|(\nabla Q)_{c,j}\right| \Delta l_j \tag{3}$$

where $(\nabla Q)_{c,j}$ is the gradient *component of the variable Q at a cell c in j coordinate direction and it is not the same as Q_c in Eq. (1) which is the cell-centered value of a variable Q at a child cell center.* Δl_j is the mesh size in j direction. Notice that the repeated index does not imply Eisenstein summation. The following conditions were used for the grid adaptation:

(1) If $\tau_{c,j} > \alpha\tau$ in any coordinate direction j, or $r_m > 1 \times 10^{-5}$, the cell is flagged to be refined.
(2) If $\tau_{c,j} \leqslant \beta\tau$ in all coordinate directions and $r_m \leqslant 1 \times 10^{-5}$ for all the cells refined from the same parent cell, these cells c are to be coarsened.

α and β are the control parameters and in this study were assumed to be 1.0 and 0.2, respectively. τ is the standard deviation calculated as

$$\tau = \left(\frac{1}{3N}\sum_{j=1}^{3}\sum_{c=1}^{N}\tau_{c,j}^2\right)^{1/2} \tag{4}$$

where N is the total number of the active cells. In addition, the difference in the refinement levels at the cell interface was limited to one to ensure a smooth transition in the refinement levels.

2.3. Adaptation for moving boundaries

Engine simulations usually need to deal with moving boundaries such as moving pistons and valves. The present flow solver rezoned inner grid points to preserve grid quality after each Lagrangian movement of the moving boundaries. The rezoning of general unstructured meshes could be accomplished by solving the Laplace equation even though it could become complicated for very complex geometries, typical of engine geometries. To avoid the difficulty in rezoning "hanging" nodes in the locally refined region, only the initial mesh (level 0) was rezoned. The new locations of the refined cells could be determined by the linear interpolation of the locations of the updated initial mesh.

3. Numerical methods

The gas phase is described by the Eulerian approach and the dispersed phase is described by the Lagrangian approach.

3.1. Governing equations of gas phase

A set of Reynolds averaged Navier–Stokes equations for reactive flows with sprays were solved in this study. Detailed information about the governing equations of the gas phase can be found in the original literature [3,24] and will not be repeated here. The gas phase equations were solved using an arbitrary Lagrangian–Eulerian methodology. The *gas phase quantities in the governing equations* were first updated in the Lagrangian phase in which *the control volume moves with the flow, and they* were then updated in the Eulerian (rezoning) phase in which the flow is frozen but cell vertices are moved to new positions and the flow field is rezoned onto the new mesh.

In the Lagrangian phase, the spray and chemical source terms were first calculated and then used to update the equations. An implicit discretization method was used to discretize the terms of thermodynamic pressure and turbulent pressure and diffusion of mass, momentum, energy and turbulence. Each discretized equation was solved iteratively using the conjugate residual method. Velocity, temperature and pressure were solved by using the SIMPLE method in an outer iteration in which the pressure field is obtained by simultaneously solving the equations for the linearized equation of state, the Lagrangian cell volume and the face volume change. The velocity was solved at the cell center to simplify numerical methods to accommodate AMR. The Rhie–Chow decoupling method was applied to address parasitic pressure oscillations resulting from the collocation of pressure and velocity at the cell center [25].

3.2. Governing equations of dispersed phase

The dispersed phase is described in the Lagrangian frame of reference. The spray distribution function [4] is statistically represented by numerous randomly sampled computational parcels, which consist of a number of drops with identical physical properties. The aerodynamic oscillations and breakup of the parcels are modeled by the Taylor-Analogy Breakup model

[6]. Collisions, coalescences, evaporation, turbulent dispersion and spray/wall interactions are modeled using corresponding sub-models [3]. Spray interacts with the gas phase by exchanging mass, momentum and energy through the coupling terms as shown in the gas phase equations. The gas phase affects the spray dynamics through aerodynamic forces, turbulent fluctuation and heat transfer. The cell-center velocity of the gas phase is used for the momentum coupling.

3.3. Boundary conditions

The boundary conditions include physical and numerical boundary conditions [3]. The physical boundaries include inflow, outflow and rigid walls. Velocity boundary conditions on rigid walls use the turbulent law-of-the-wall condition. Available temperature boundary conditions include adiabatic walls and fixed temperature walls.

3.4. Diffusive fluxes

Due to the use of AMR, the calculation of diffusive fluxes needed to be modified from its original algorithm to account for the coarse-fine mesh interface introduced by AMR. Terms bearing a format of $\int_S \nabla Q \cdot d\mathbf{A}$ in the gas phase equations were approximated by using the mid-point quadrature rule,

$$\int_S \nabla Q \cdot d\mathbf{A} \approx \sum_f (\nabla Q)_f \cdot \mathbf{A}_f \tag{5}$$

where subscript f represents a cell face. For a conventional face f in Fig. 2(a), the term $(\nabla Q)_f \cdot \mathbf{A}_f$ was approximated by

$$(\nabla Q)_f \cdot \mathbf{A}_f = a_{c,cn}(Q_c - Q_{cn}) + a_{1,2}(Q_1 - Q_2) + a_{4,3}(Q_4 - Q_3) \tag{6}$$

where Q_c, Q_{cn} are the cell-centered values of cell c and cell cn and Q_1, Q_2, Q_3, Q_4 are the edge-centered values of edges 1, 2, 3 and 4. The edge-centered values were obtained by averaging the cell-centered values of all cells that share the edge. $a_{c,cn}$, $a_{1,2}$ and $a_{4,3}$ were the geometric coefficients and determined by solving a system of 3×3 equations [3,24]. At the coarse-fine interface, Eq. (6) was applied to the l-level child cells (cells c_2, c_3 in Fig. 2(b)). When calculating the edge-centered values Q_i (i.e., the dashed edge in the cell c_2), the contribution from the $(l-1)$-level cell (i.e., the cell c_1) across the interface was achieved by attaching the edge to the $(l-1)$-level cell, which is done during the mesh refinement. The term $\nabla Q \cdot \mathbf{A}$ for the face of the $(l-1)$ -level cell became

$$(\nabla Q \cdot \mathbf{A})_{l-1} \approx -\sum_h (\nabla Q \cdot \mathbf{A})_{h,l} \tag{7}$$

where $(\nabla Q \cdot \mathbf{A})_{h,l}$ is the value for one of the l-level cells.

The viscous stress tensor term $\int_s \boldsymbol{\sigma} \cdot dA$ in the momentum equations was approximated by summing over all the cell faces

$$\int_s \boldsymbol{\sigma} \cdot dA \approx \sum_f \boldsymbol{\sigma}_f \cdot \mathbf{A}_f \tag{8}$$

where $\boldsymbol{\sigma}_f$ is the viscous stress tensor,

$$\boldsymbol{\sigma}_f = \mu_t \left[\nabla \mathbf{u} + (\nabla \mathbf{u})^T\right] - \frac{2}{3}\mu_t \nabla \cdot \mathbf{u}\mathbf{I} \tag{9}$$

with μ_t as the *effective* viscosity and $\mathbf{I}$ as the unit tensor. One must find the value of $\boldsymbol{\sigma}_f$ and thus the velocity gradients $(\nabla u)_f$ at each cell face. For a velocity component u and a face f in Fig. 2(a), the gradients ∇u satisfy the following condition:

$$\mathbf{X}(\nabla u)^T = \Delta u \tag{10}$$

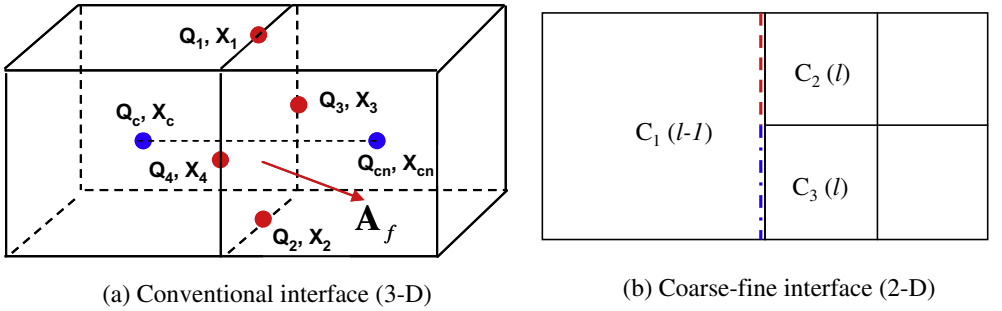

(a) Conventional interface (3-D) (b) Coarse-fine interface (2-D)

Fig. 2. Geometric arrangement of the gradient calculation at an interface f.

where the matrix $\mathbf{X}$ is defined by

$$\mathbf{X} = \begin{pmatrix} x_{ccn} & y_{ccn} & z_{ccn} \\ x_{12} & y_{12} & z_{12} \\ x_{43} & y_{43} & z_{43} \end{pmatrix}, \tag{11}$$

where x_{ij}, y_{ij} and z_{ij} are the components of the vectors $\mathbf{x}_{ij}$, $\mathbf{y}_{ij}$ and $\mathbf{z}_{ij}$, respectively, and the right-hand side vector Δu has

$$\Delta u = \begin{pmatrix} u_c - u_{cn} \\ u_1 - u_2 \\ u_4 - u_3 \end{pmatrix}. \tag{12}$$

Then the components of the gradients ∇u in each coordinate direction could be determined as follows:

$$\begin{aligned} (\nabla u)_x &= \mathbf{i} \cdot \nabla u = \left(\mathbf{i} \cdot \mathbf{X}^{-1}\right) \Delta u \\ (\nabla u)_y &= \mathbf{j} \cdot \nabla u = \left(\mathbf{j} \cdot \mathbf{X}^{-1}\right) \Delta u \\ (\nabla u)_z &= \mathbf{k} \cdot \nabla u = \left(\mathbf{k} \cdot \mathbf{X}^{-1}\right) \Delta u \end{aligned} \tag{13}$$

where $\mathbf{i}$, $\mathbf{j}$, $\mathbf{k}$ are the unit vectors in x, y and z coordinate directions, respectively. The terms $\mathbf{i} \cdot \mathbf{X}^{-1}$, $\mathbf{j} \cdot \mathbf{X}^{-1}$ and $\mathbf{k} \cdot \mathbf{X}^{-1}$ correspond to the 1st, 2nd and 3rd rows of the matrix $\mathbf{X}^{-1}$, respectively, and could be readily obtained from *the geometric coefficients [3,24]*. The gradients of other velocity components were calculated in a similar way. Then, the viscous diffusion term $\boldsymbol{\sigma}_f \cdot \mathbf{A}_f$ for the face of a l-level cell could be determined at the interface. For the face of the $(l-1)$-level cell across the interface, this term was obtained by summing the terms for all the l-level cells as

$$\left(\boldsymbol{\sigma}_f \cdot \mathbf{A}_f\right)_{l-1} \approx -\sum_h \left(\boldsymbol{\sigma}_f \cdot \mathrm{A}_f\right)_{h,l} \tag{14}$$

where h represents an l-level cell at the interface.

One also needs to calculate viscous dissipation of mean flow kinetic energy $\int_V \boldsymbol{\sigma} : \nabla \mathbf{u}\, dV$ since both tensors $\boldsymbol{\sigma}$ and $\nabla \mathbf{u}$ are evaluated at the cell center instead of the cell faces. Let u be a component of velocity $\mathbf{u}$, then ∇u at the cell center is approximated as a cell-wise constant using the divergence theorem as

$$\nabla u \approx \frac{1}{V}\int_V \nabla u\, dV = \frac{1}{V}\int_S u\, d\mathbf{A} \approx \frac{1}{V}\sum_f u_f \mathbf{A}_f \approx \frac{1}{V}\sum_f \frac{1}{2}\left(u_{c,l} + u_{c,l-1}\right)\mathbf{A}_f \tag{15}$$

where u_f is the face center velocity and $u_{c,l}$, $u_{c,l-1}$ are the cell-centered values at the levels l and $(l-1)$, respectively. At the coarse-fine interface, for an l-level cell, u_f is simply approximated by the average of the cell-center values $u_{c,l}$ and $u_{c,l-1}$. For the $(l-1)$-level cell across the interface, $u_{c,l}$ is the average of the cell-centered values of all the l-level cells sharing the interface. After the gradient terms are determined at the cell center, $\boldsymbol{\sigma}$ can be determined accordingly.

The collocation of pressure and velocity can cause parasitic pressure oscillations due to velocity–pressure decoupling [26]. To reduce the oscillations, we adopted the Rhie–Chow method [25] when computing the face volume change for the pressure iterations in the Lagrangian phase. Using this technique, the face volume change $(\mathbf{u} \cdot \mathbf{A})_f$ was modified by pressure gradients according to the following expression:

$$(\mathbf{u} \cdot \mathbf{A})_f^L = (\mathbf{u} \cdot \mathbf{A})_f^{L_o} - \frac{\Delta t}{\frac{1}{2}(\rho_c + \rho_{cn})}\left\{(\nabla p)_f - \frac{1}{2}\left[(\nabla p)_c + (\nabla p)_{cn}\right]\right\} \cdot \mathbf{A}_f \tag{16}$$

where $(\mathbf{u} \cdot \mathbf{A})_f^{L_o}$ is calculated from the original face volume change equation that is derived from the momentum balance for control volume centered around the face f [3,24]. $(\nabla p)_f$ is the pressure gradient at the cell face and was determined by using the method in Eq. (6). $(\nabla p)_c$, $(\nabla\ p)_{cn}$ are the cell pressure gradients and are calculated by the divergence theorem

$$\nabla p \approx \frac{1}{V}\int_V \nabla p\, dV = \frac{1}{V}\int_S p\, d\mathbf{A} \approx \frac{1}{V}\sum_f p_f \mathbf{A}_f \approx \frac{1}{V}\sum_f \frac{1}{2}\left(p_{c,l} + p_{cn,l-1}\right)\mathbf{A}_f \tag{17}$$

where $p_{c,l}$ and $p_{cn,\ l-1}$ are the cell-center pressures. $p_{c,\ l}$ and $p_{cn,l-1}$ were determined in the same way as $u_{c,l}$ and $u_{c,l-1}$ in Eq. (15), while Eq. (17) was calculated for the cells on both sides of the interface. The face volume change for the $(l-1)$-level cell across the interface was then summed over all the l-level cells on the other side of the interface as

$$(u \cdot \mathbf{A})_{f_{l-1}}^L \approx -\sum_h (u \cdot \mathbf{A})_{h,f_l}^L. \tag{18}$$

The term $(\mathbf{u} \cdot \mathbf{A})_f^L$ was used to calculate the Lagrangian cell volume V^L that appeared in the pressure iteration *and also used to calculate the convective face volume change δV_f when a face moved from its Lagrangian position to the final position corresponding to the new time step.*

3.5. Convective fluxes

In the calculation of convective fluxes, the presence of the unconventional coarse-fine interface resulting from AMR also needs to be considered. In the transient engine simulation, after the mesh moved with the fluid in the Lagrangian phase, the mesh was rezoned to the new location, which led to the convective transport of the flow fields due to the relative movement of the mesh to the frozen fluid. The convective fluxes in the Eulerian phase were explicitly sub-cycled within the main computational time step to save computer time. *The sub-cycled time step Δt_c was an integral sub-multiple of the main computational time step Δt. At each sub-cycle v, the face volume change δV_f at the coarse-fine interface was calculated based on the face f of the l-level cell from the location at time n to the final location at time n + 1.* The $\delta V_{f_{l-1}}$ for the $(l-1)$-level cell at the interface was obtained by taking the negative of the sum of δV_{f_l} for the corresponding l-level cells. If δV_f was positive the face movement led to the cell volume expansion or, if it was negative, to the cell volume compression.

The flux through a conventional face f into a cell c shown in Fig. 3(a) was calculated by

$$(\rho q V)_c^v = (\rho q V)_c^{v-1} + (\rho q)_f^{v-1} \delta V_{f_l} \tag{19}$$

where ρ is the density, V is the cell volume and q represents the cell-centered quantity being evaluated such as velocity components, specific internal energy, etc. The quantity $(\rho q)_f$ at each sub-cycle was determined by using a quasi-second-order upwind (QSOU) scheme [3,24]

$$(\rho q)_f = (\rho q)_{c_n} + \frac{d(\rho q)}{ds} |\mathbf{x}_f - \mathbf{x}_{c_n}| \left(1 - \frac{|\delta V_f|}{V_{c_n}}\right) \tag{20}$$

where $\frac{d(\rho q)}{ds}$ is the slope in each cell computed by using a strong monotone upwind scheme modified from Van Leer's upwind scheme [29] as

$$\frac{d(\rho q)}{ds} = sign((\rho q)_c - (\rho q)_{c_n}) \min\left(\frac{|(\rho q)_c - (\rho q)_{c_n}|}{|\mathbf{x}_c - \mathbf{x}_{c_n}|}, \frac{|(\rho q)_{c_n} - (\rho q)_{c_{no}}|}{|\mathbf{x}_{c_n} - \mathbf{x}_{c_{no}}|}\right) \tag{21}$$

where $\mathbf{x}_c, \mathbf{x}_{c_n}, \mathbf{x}_{c_{no}}$ represent the cell-centered locations at the new time level while $\mathbf{x}_f$ is the face center. $\mathbf{x}_L$ is the Lagrangian position of the face. $\frac{d(\rho q)}{ds}$ is zero if $(\rho q)_c - (\rho q)_{c_n}$ and $(\rho q)_{c_n} - (\rho q)_{c_{no}}$ have different signs. For $\frac{d(\rho q)}{ds}$ of the $(l-1)$-level cell (i.e., c_1 in Fig. 3(b)), $(\rho q)_{c_n}$ and $\mathbf{x}_{c_n}$ are the average values of all the l-level cells (i.e., c_2 and c_3) on the other side. Only the faces from the l-level cells were looped over to avoid a duplicate flux, and $\frac{d(\rho q)}{ds}$ was determined for every face based on its associated volume change δV_f. Eq. (19) was then applied to the l-level cells. The flux for the $(l-1)$-level cell is given by

$$(\rho q V)_{f_{l-1}}^v = (\rho q V)_{f_{l-1}}^{v-1} - \sum_h (\rho q)_{f_{h,l}}^{v-1} \delta V_{f_{h,l}} \tag{22}$$

where $\sum_h$ means summation over all the l-level cells at the interface.

3.6. Time step constraint

The new time step Δt^{n+1} was the minimum among an array of time step constraints [3]. Two constraints needed to be re-evaluated on the refined cells when AMR was used. First, the time step must be restricted to limit the cell distortion due to mesh movement in the Lagrangian phase. This constraint *used the rate of strain tensor S_{ij} and thus the gradient ∇u, which needed to consider the coarse-fine interface, was calculated using* Eq. (15). Second, the convection time step must reflect the cell size change resulting from the refinement/coarsening. The convection time step was limited by

$$\Delta t_c^n \leqslant C_c \Delta t_c^{n-1} \min_f \frac{V}{|\delta V_f|} \tag{23}$$

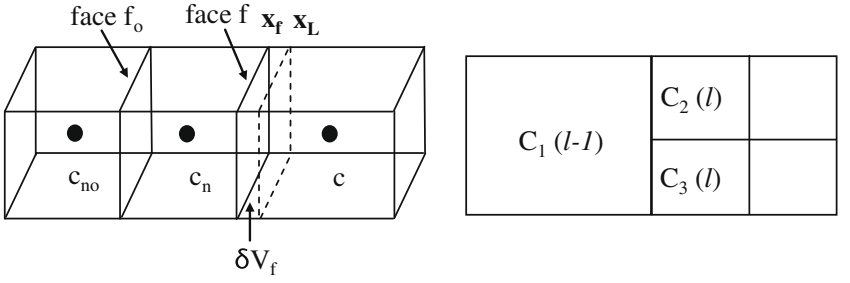

(a) Conventional interface (3-D) (b) Coarse-fine interface (2-D)

Fig. 3. Computational stencil for gradient calculation.

where C_c is a constant 0.2, V is the cell volume, Δt_c^{n-1} is the previous time step and δV_f is the face volume change. Unfortunately, δV_f was not available for the newly refined cells using AMR since this term was calculated in the rezoning stage, whereas Eq. (23) was calculated at the beginning of each computational cycle. For the newly refined cells, Δt_c^n could be approximated by using geometrical relationships. For a child cell, its volume was approximately one-eighth of its parent's volume, and its face volume change was approximately one-fourth of that of its parent cell. The convection time step of each child cell could be taken as half of the time step for the parent cell. In the cell coarsening, the face volume change δV_f for the re-activated parent cell could be approximated from its child cells. Then Eq. (23) could be directly applied.

4. Numerical results

4.1. Spray simulations in a cylindrical combustion chamber

The present mesh adaptation method was applied to simulate an engine spray under transient conditions. The engine had a cylindrical combustion chamber with the bore and stroke equal to 10 cm and 10 cm, respectively. The engine speed was 4000 rev/min. The spray was injected at a constant rate of 135 m/s into the chamber from the center of the cylinder head. The initial drop diameter was 200 μm, and the initial drop temperature was 301 K. The fuel was iso-octane and the injected fuel was 3.6 mg. The ambient was air with an initial temperature of 301 K and pressure of 1 bar. Spray dynamics were modeled using various sub-models for breakup, collision, turbulent dispersion, spray/wall interactions and evaporation [3,24]. The initial mesh was based on the Cartesian O-grid type mesh. The turbulent law-of-the-wall boundary conditions were used to treat turbulence and heat transfer near walls. The fixed temperature condition was used for wall temperature. The initial spray conditions were determined from the injector geometry and injection conditions. The injection timing was based on crank angle degree after top-dead-center (ATDC), as is the standard terminology in reciprocating engine simulation. The simulation started from 180 ATDC when the piston started to move upward, and the fuel was injected also at 180 ATDC for a duration of 30 crank angle degrees.

It should be noted that the key to assess AMR is that a coarse mesh using AMR should give the same results as the uniformly fine mesh but with reduced computer time. Therefore, results using the uniformly fine mesh will serve as the baseline for AMR verification. Notice that in this paper, "coarse" and "fine" are only relative terms for describing the mesh density. The coarsest mesh size was 5 mm. To meet the large void fraction condition of the Lagrangian method, AMR was performed up to 2 levels in this study. Simulations were performed for the following mesh conditions: 5 mm, 2.5 mm, 1.25 mm, 5 mm with one-level refinement (5 mm + L1) and 5 mm with two-level refinement (5 mm + L2). Note that the "5 mm + L1" case would have the comparable mesh size in the spray region as the "2.5 mm" case, and the "5 mm + L2" case would have the comparable mesh size as the "1.25 mm" case.

Due to the stochastic nature of spray modeling, comparisons using representative statistical data of spray would not be feasible. Therefore, we chose the liquid and vapor penetrations, vapor mass fraction and spray structure as parameters for comparison. The liquid penetration was defined as the distance from the nozzle orifice to a position that corresponds to 95% of the integrated amount of liquid drops from the nozzle orifice. The vapor penetration was the axial distance from the nozzle orifice to a position with the vapor mass fraction greater than 0.01.

Fig. 4 shows the comparisons of liquid and vapor penetrations for the five cases studied. The "5 mm + L1" case produced similar penetrations to those using 2.5 mm mesh size. The "5 mm + L2" case produced comparable penetrations to those using 1.25 mm mesh size. It can be seen that the case using 5 mm mesh size without AMR produced the shortest penetrations. As the mesh density increased, so did the penetrations because the increased grid resolution improved the prediction

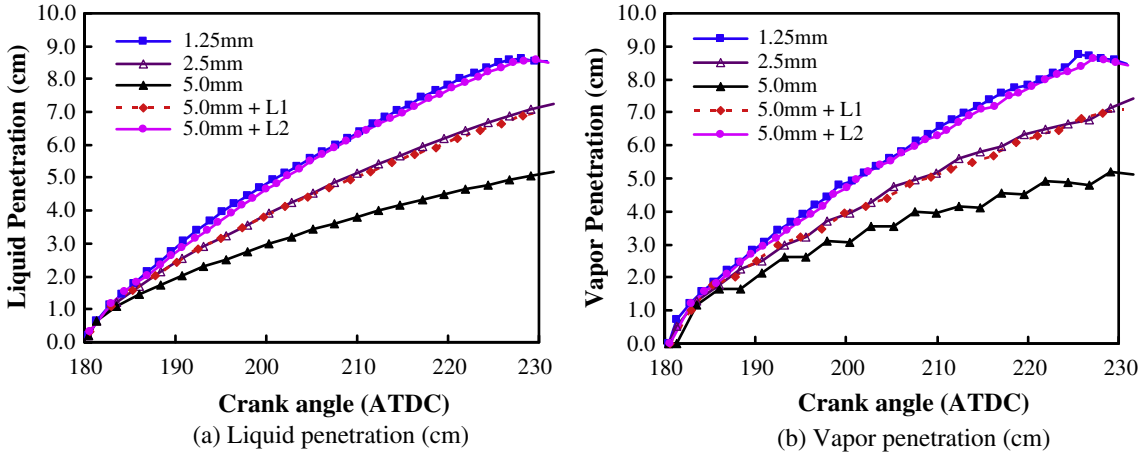

Fig. 4. Comparison of liquid and vapor penetrations using different meshes with respective refinement levels.

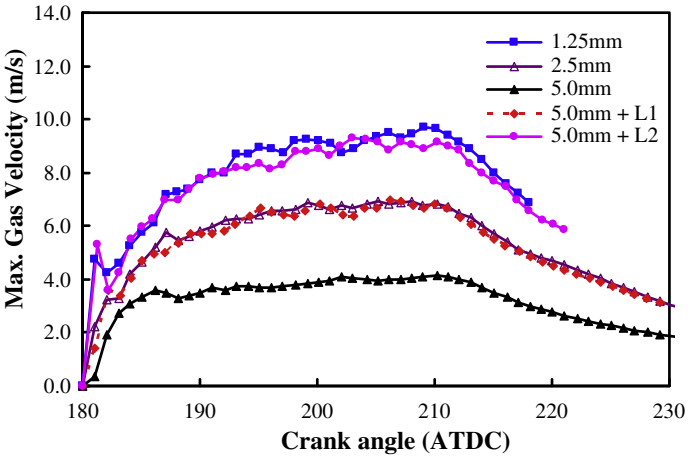

Fig. 5. Comparison of the maximum gas velocity for different mesh refinement conditions.

Table 1
Comparison of the computer time for different mesh sizes.

Mesh size Δx	1.25 mm	2.5 mm	5 mm	5 mm + L1	5 mm + L2
Time (min)	4770.9	311.3	15.4	88.5	467.2
% (Based on the 1.25 mm mesh case)	100.0	6.52	0.32	1.85	9.79

in momentum exchange from the spray to the gas phase, resulting in smaller relative velocities and thus longer penetrations, as can be seen from the maximum gas velocity prediction in Fig. 5. Table 1 shows the comparisons of computer times for the cases studied for computations from 180 to 360 ATDC (i.e., piston at top-dead-center). It can be seen that the time saving for both level 1 and level 2 refinements are significant compared to the equivalent fine mesh cases for the same level of solution accuracy.

Fig. 6 shows the fuel vapor distribution and spray pattern for the five cases on a cutplane along the spray axis at 205 ATDC with all the drops projected onto the cutplane. Similar fuel vapor distributions can be observed between the "5 mm + L1" case and the "2.5 mm" case. The same is true for the results between the "5 mm + L2" case and the "1.25 mm" case. In the "5.0 mm" case, fuel vapor was distributed in a wider region than in other cases due to over-estimated diffusion resulting from the coarse grid size. Due to the insufficient spatial resolution, the "5.0 mm" case produced the so-called "clover leaf" artifact (Fig. 7(c) bottom) [10,12]. The artifact is a result of drop collisions that move the new drops toward the cell centers

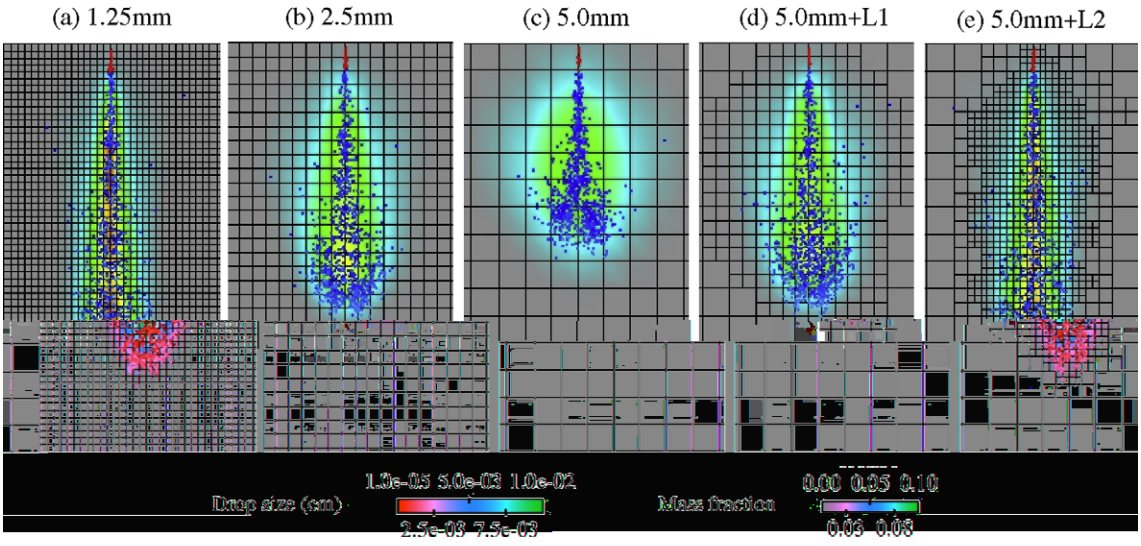

Fig. 6. Comparison of the spray pattern and fuel vapor on a cutplane along the spray axis at 205 ATDC.

around the injector, since the drops moving 90° apart in the same cell tended to move toward the cell center due to the large relative velocities between the drops. AMR algorithms refined all the cells around the injector and thus distributed drops into more cells, alleviated this artifact and produced the pattern similar to that using the fine mesh as seen in Fig. 7(a, b, d, e).

It can be seen that the spray simulation is mesh dependent in a coarse mesh if AMR is not used, which can also be found in the literature [10–15]. To further demonstrate the benefits of using AMR, we performed simulations in the same domain by injecting spray at a 40° angle from the vertical axis. The ambient pressure was 3 bars. Simulations were performed on the 1.25 mm, 5.0 mm and 5.0 mm + L2 refinement. Fig. 8 shows the comparisons of spray structures and vapor contours at 1 ms after injection. The coarse mesh without AMR (5.0 mm) predicted a shorter penetration and higher vapor diffusion than those using the fine mesh or the coarse mesh with AMR. It can also be seen that the coarse mesh without AMR predicted asymmetric shear stresses on the top and bottom of the spray tip, causing an asymmetric spray structure. The results using the 5 mm + L2 refinement were comparable to those using the 1.25 mm mesh.

The above comparisons indicate that the present AMR method can produce comparable results to those using the fine mesh but with much less computer time (less than 10% of the time for the corresponding fine mesh). In particular, AMR refines all cells that contain large drops or have high vapor gradients. AMR can also effectively alleviate the "clover leaf" artifact and other artifacts in the Cartesian mesh. Therefore, the benefits of using AMR are evident and the implementation is verified. *Note that the use of AMR could influence the drop collision and vaporization calculation. The frequency and probability of*

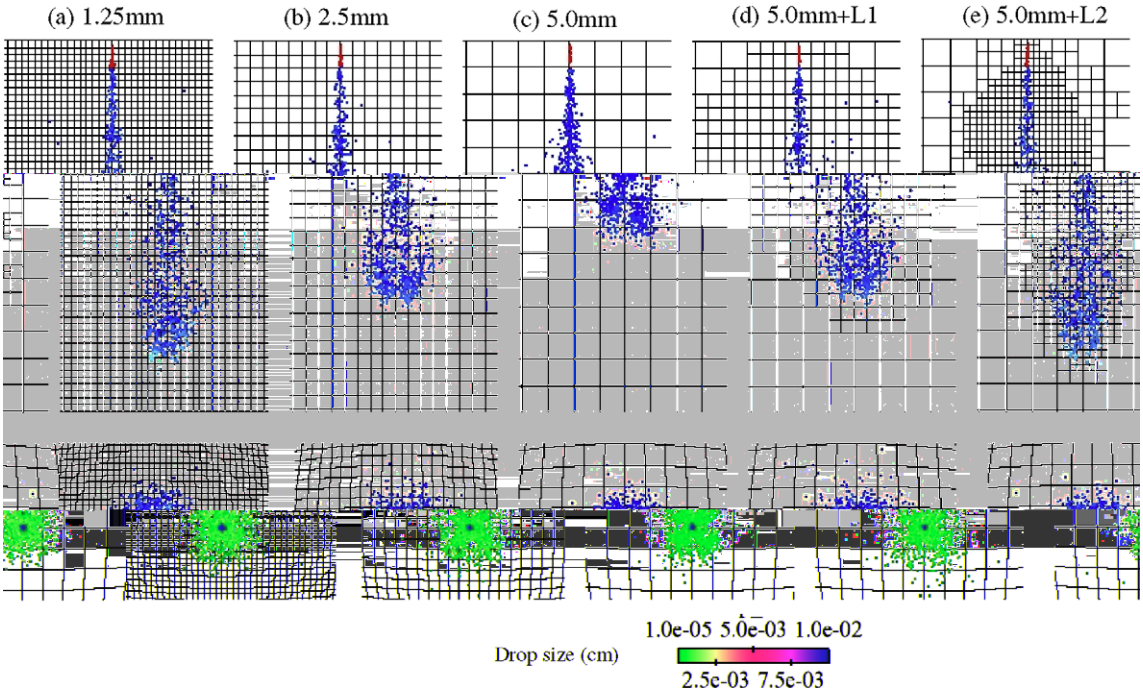

Fig. 7. Comparison of the spray pattern on a cutplane along the spray axis (top) and at 3.0 cm above the piston surface (bottom) at 205 ATDC.

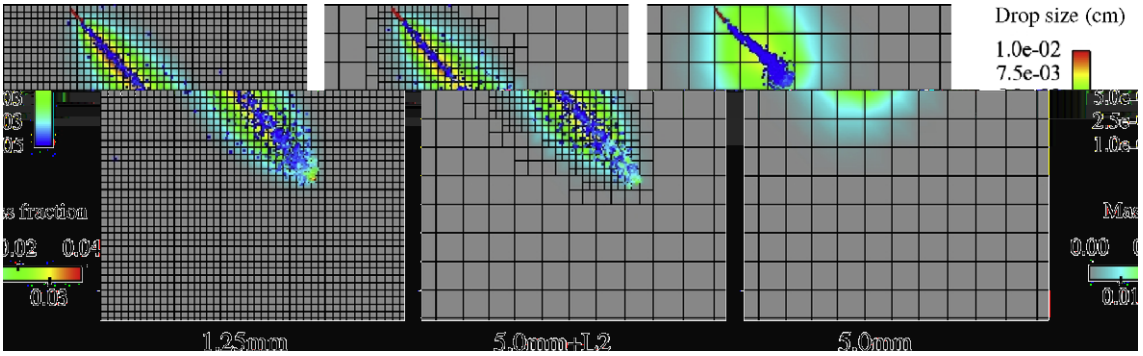

Fig. 8. Comparison of the spray pattern and fuel vapor for injection with a 40° angle from the vertical axis.

drop collisions could be altered due to the dynamically changing cell size. The change in the cell size also changes the amount of gas phase energy that is available for drop vaporization and thus could affect the predicted drop vaporization rate. Therefore, adjustments to spray model constants may be possible although it was not required in this study. Additionally, the quality of the refined cells may also be a concern if AMR is performed on a cell that already has a high aspect ratio. If a low-quality cell is further refined by AMR during simulation, the quality of the child cells will further deteriorate and may cause numerical difficulties.

The accuracy of spray modeling depends on both the grid resolution and the spray model itself. It is known that a fine mesh would generally result in more accurate solutions in the Lagrangian–Eulerian approach for spray modeling [15].The purpose of the present AMR algorithm is to avoid the use of an overly fine mesh in order to improve computational efficiency. The success of AMR depends largely on the accurate modeling of liquid-to-gas and gas-to-liquid couplings. In practical applications, a sufficiently fine mesh that has a grid size of 0.5–1 mm is often required for accurate engine spray simulation [15,30]. This study used two-level refinement to achieve reasonable grid resolution for engine spray application. Nonetheless, more refinement levels may be applied in order to obtain a higher grid resolution for specific applications.

5. Conclusion

Dynamic mesh refinement algorithms based on the normalized fuel mass and the gradients of vapor mass fraction were developed and implemented into the unstructured collocated KIVA-4. The mesh refinement strategy can increase the spatial resolution in the spray region and improve the exchanges of mass and momentum between the liquid and gas phases. The edge-based and face-based algorithms in the solver were properly modified to resolve the coarse-fine cell interface in hydrodynamic calculation. Mesh rezoning with moving boundaries was simplified by applying rezoning to the initial mesh and then performing interpolation to obtain the new locations of the refined cells. The interpolation cost was modest compared to the expensive iterative rezoning method. The present AMR approach was applied to simulate an engine spray in a combustion chamber with refinement up to two levels. The simulations demonstrated the effectiveness of AMR in producing the results with the same level of accuracy as those using the uniformly fine mesh without AMR. The computer time for the simulations using AMR only amounted to 10% of the time using the uniformly fine mesh with the corresponding level of grid resolution.

Due to the increased spatial resolution resulting from AMR, not only can the Eulerian fields of gas phase be computed more accurately in the vicinity of liquid drops due to the reduced truncation errors, but the interphase coupling between the two phases can also be improved, indicating the improvement from both gas-to-liquid and liquid-to-gas couplings. The over-estimated diffusion of momentum and fuel vapor due to the insufficient spatial resolution can be significantly reduced. It was found that AMR can alleviate grid-dependent artifacts associated with the modeling of particle collisions and evaporation. As a result, AMR can give a greater flexibility in providing appropriate grid resolution for the Lagrangian spray modeling than using the uniformly fine meshes with reduced computer time.

Acknowledgments

The authors acknowledge the financial support of Ford Motor Company. Helpful comments by Dr. David Torres at Los Alamos National Laboratory during the course of this work are also greatly appreciated.

References

[1] J.K. Dukowicz, A particle-fluid numerical model for liquid sprays, J. Comp. Phys. 35 (1980) 229–253.
[2] R.D. Reitz, C.J. Rutland, Development and testing of diesel engine CFD models, Prog. Energy Combust. Sci. 21 (1995) 173–196.
[3] A.A. Amsden, P.J. O'Rourke, T.D. Butler, KIVA-II: A Computer Program for Chemically Reactive Flows with Sprays, Technical Report, Los Alamos National Laboratory, LA-11560-MS, 1998.
[4] F.A. Williams, Spray combustion and atomization, Phys. Fluids 1 (6) (1958) 541–544.
[5] G.M. Faeth, Evaporation and combustion of sprays, Prog. Energy Combust. Sci. 9 (1983) 1–76.
[6] P.J. O'Rourke, A.A. Amsden, The Tab Method for Numerical Calculation of Spray Droplet Breakup, SAE Technical Paper, 872089, 1987.
[7] P.J. O'Rourke, Statistical properties and numerical implementation of a model for droplet dispersion in a turbulent gas, J. Comp. Phys. 83 (1989) 345–360.
[8] S. Subramaniam, P.J. O'Rourke, Numerical Convergence of the KIVA-3 Code for Aprays and Its Implications for Modeling, Technical Report, Los Alamos National Laboratory, LAUR 98-5465, 1998.
[9] P. Beard, J.M. Duclos, C. Habchi, G. Bruneaux, K. Mokkadem, T. Baritaud, Extension of Lagrangian–Eulerian Spray Modeling: Application to High Pressure Evaporating Diesel Spray, SAE Technical Paper 2000-01-1893, 2000.
[10] S. Hieber, An Investigation of the Mesh Dependence of the Stochastic Droplet Applied to Dense Liquid Sprays, Master's Thesis, Mathematics Department, Michigan Technological Univ., 2001.
[11] R. Aneja, J. Abraham, How far does the liquid penetrate in a diesel engine: computed results vs. measurements?, Combust Sci. Technol. 138 (1998) 233–255.
[12] D.P. Schmidt, C.J. Rutland, A new droplet collision algorithm, J. Comp. Phys. 164 (2000) 62–80.
[13] S. Are, S. Hou, D.P. Schmidt, Second-order spatial accuracy in Lagrangian–Eulerian spray calculations, Numer. Heat Transfer, Part B 48 (2005) 25–44.
[14] S. Tonini, M. Gavaises, A. Theodorakakos, Modelling of high-pressure dense diesel sprays with adaptive local grid refinement, Int. J. Heat Fluid Flow 29 (2008) 427–448.
[15] J. Abraham, What Is Adequate Resolution in the Numerical Computation of Transient Jets? SAE Technical Paper, 970051, 1997.
[16] C. Baumgarten, Mixture Formation in Internal Combustion Engines, Springer, 2006.
[17] N. Sterno, G. Greeves, S. Tullis, X. Jiang, H. Zhao, Improvements of the KIVA Dense Spray Modeling for HSDI Diesel Engines, SAE Technical Papers, 2007-01-0001, 2007.
[18] D.P. Schmidt, C.J. Rutland, Reducing grid dependence in droplet collision calculations, ASME J. Eng. Gas Turbine Power 126 (2) (2004) 227–233.

[19] V.I. Golovitchev, N. Nordin, Detailed chemistry spray combustion model for the KIVA code, in: Proceedings of the 11th International Multidimensional Engine Modeling User's Group Meeting at the SAE Congress, 2001, pp. 1–6.
[20] A.M. Lippert, S. Chang, S. Are, D.P. Schmidt, Mesh Independence and Adaptive Mesh Refinement for Advanced Engine Spray Simulations, SAE Technical Paper, 2005-01-0207, 2005.
[21] J. Bell, M.J. Berger, J. Saltzman, M. Welcome, Three-dimensional adaptive mesh refinement for hyperbolic conservation laws, SIAM J. Sci. Comput. 15 (1994) 127–138.
[22] R.W. Anderson, N.S. Elliott, R.B. Pember, An arbitrary Lagrangian–Eulerian method with adaptive mesh refinement for the solution of the Euler equations, J. Comp. Phys. 199 (2004) 598–617.
[23] P.K. Senecal, K.J. Richards, E. Pomraning, T. Yang, M.Z. Dai, R.M. McDavid, M.A. Patterson, S. Hou, T. Shethaji, A New Parallel Cut-cell Cartesian CFD Code for Rapid Grid Generation Applied to In-cylinder Diesel Engine Simulations, SAE Technical Papers, 2007-01-0159, 2007.
[24] D.J. Torres, M.F. Trujillo, KIVA-4: an unstructured ALE code for compressible gas flow with sprays, J. Comp. Phys. 219 (2) (2006) 943–975.
[25] Y. Tsui, Y. Pan, A pressure–correction method for incompressible flows using unstructured meshes, Numer. Heat Transfer, Part B 49 (2006) 43–65.
[26] J.H. Ferziger, M. Peric, Computational Methods for Fluid Dynamics, third ed., Springer, 2000.
[27] H. Jasak, A.D. Gosman, Automatic resolution control for the finite volume method, Part 2: Adaptive mesh refinement and coarsening, Numer. Heat Transfer, Part B 38 (2000) 257–271.
[28] Z.J. Wang, R.F. Chen, Anisotropic solution-adaptive viscous cartesian grid method for turbulent flow simulation, AIAA J. 40 (10) (2002) 1969–1978.
[29] B. Van Leer, Towards the ultimate conservative difference scheme V. A second-order sequel to Godunov's method, J. Comp. Phys. 32 (1979) 101–136.
[30] P. Beard, O. Colin, M. Miche, Improved Modeling of DI Diesel Engines Using Sub-Grid Description of Spray and Combustion, SAE Paper 2003-01-0008, 2003.